

Article

# Development of Seasonal BRDF Models to Extend the Use of Deep Convective Clouds as Invariant Targets for Satellite SWIR-Band Calibration

Rajendra Bhatt <sup>1,\*</sup>, David R. Doelling <sup>2</sup>, Benjamin Scarino <sup>1</sup>, Conor Haney <sup>1</sup> and Arun Gopalan <sup>1</sup>

<sup>1</sup> Science Systems and Applications Inc., 1 Enterprise Pkwy, Hampton, VA 23666, USA; benjamin.r.scarino@nasa.gov (B.S.); conor.o.haney@nasa.gov (C.H.); arun.gopalan-1@nasa.gov (A.G.)

<sup>2</sup> NASA Langley Research Center, Hampton, VA 23666, USA; david.r.doelling@nasa.gov

\* Correspondence: rajendra.bhatt@nasa.gov; Tel.: +1-757-951-1656; Fax: +1-757-951-1902

Received: 8 September 2017; Accepted: 13 October 2017; Published: 18 October 2017

**Abstract:** Tropical deep convective clouds (DCC) are an excellent invariant target for vicarious calibration of satellite visible (VIS) and near-infrared (NIR) solar bands. The DCC technique (DCCT) is a statistical approach that collectively analyzes all identified DCC pixels on a monthly basis. The DCC reflectance in VIS and NIR spectrums is mainly a function of cloud optical depth, and provides a stable monthly statistical mode. However, for absorption shortwave infrared (SWIR) bands, the monthly DCC response is found to exhibit large seasonal cycles that make the implementation of the DCCT more challenging at these wavelengths. The seasonality assumption was tested using the SNPP-VIIRS SWIR bands, with up to 50% of the monthly DCC response temporal variation removed through deseasonalization. In this article, a monthly DCC bidirectional reflectance distribution function (BRDF) approach is proposed, which is found to be comparable to or can outperform the effects of deseasonalization alone. To demonstrate that the SNPP-VIIRS DCC BRDF can be applied to other JPSS VIIRS imagers in the same 13:30 sun-synchronous orbit, the VIIRS DCC BRDF was applied to Aqua-MODIS. The Aqua-MODIS SWIR band DCC reflectance natural variability is reduced by up to 45% after applying the VIIRS-based monthly DCC BRDFs.

**Keywords:** calibration; DCC; BRDF; SWIR bands; VIIRS; MODIS; JPSS

## 1. Introduction

In 2017, NOAA began on the follow-on Joint Polar Satellite System (JPSS)-3 and JPSS-4 satellites, each having 5–6 instruments [1]. The constellation of JPSS satellites (projected launch dates) including the Suomi National Polar-orbiting Operational Environmental Satellite System (NPOESS) Preparatory Project (SNPP) (28 October 2011), JPSS-1 (2017), JPSS-2 (2022), JPSS-3 (2026), and JPSS-4 (2031) should provide coverage into 2030, primarily for the purpose of weather observations [2]. The JPSS satellites will all be launched into the same 13:30 ascending sun-synchronous orbit at an altitude of 824 km. This is similar to the operational procedure of the MetOp program [3], where both Metop-A and -B satellites are in the same 09:30 descending sun-synchronous orbit at the same altitude as JPSS. The ~830-km orbit holds an altitude at which an imaging radiometer, such as Visible Infrared Imaging Radiometer Suite (VIIRS), can contiguously scan a zone across the equator without any spatial gaps.

The NASA Clouds and the Earth's Radiant Energy System (CERES) instrument is planned for each of the JPSS satellites. This implementation will allow the CERES program [4] to have a continuous 40-year record of broadband flux by year 2040. The CERES broadband flux record must be of climate quality to be useful for climate model validation as well as assuredly monitor the net flux balance of the Earth's emitted longwave and incoming absorbed shortwave radiation. CERES relies on angular directional models based on scene type, i.e., surface conditions and cloud coverage, to convert CERES

observed radiances into fluxes. The scene type is determined by the VIIRS imager, which is also onboard the JPSS satellites. The VIIRS imager must be free of any calibration drifts in order to provide consistent scene conditions over the record. The CERES Edition 3 fluxes were impacted by a Moderate Resolution Imaging Spectroradiometer (MODIS) imager band 1 (0.65  $\mu\text{m}$ ) collection 5 calibration drift of 2% [5], which reduced the cloud optical depth over time, and thereby changed the scene selection, causing a reduction in the CERES shortwave (SW) flux by  $-0.25 \text{ Wm}^{-2}$  [6]. This reduction is close to the SW flux stability requirement for climate accuracy, i.e.,  $0.3 \text{ Wm}^{-2}/\text{decade}$  [7]. By injecting the satellites into the same orbit ( $\sim 100$ -min period), but at half-an-orbit ( $\sim 50$  min) apart will prevent any inter-calibration between JPSS sensors that uses coincident measurements. Therefore, the JPSS satellite sensors will need to rely on onboard calibration and invariant Earth and lunar targets to monitor any residual on orbit calibration drifts. Just as important as assessing the stability, the series of VIIRS sensors must also be inter-calibrated to radiometrically scale the individual instruments to a common calibration reference. Doing so will ensure that there are no discontinuities in the flux or cloud retrievals for CERES products spanning multiple VIIRS sensors. This inter-series continuity will be the topic of a follow-on paper.

The CERES program will depend on deep convective clouds (DCC) to evaluate the stability of the individual JPSS VIIRS imagers. The CERES VIIRS cloud mask and retrieval algorithm relies on both the visible and near-IR (VIS-NIR) (defined here as  $<1 \mu\text{m}$ ) and shortwave infrared (SWIR) (defined here as  $>1 \mu\text{m}$ ) bands. The DCC reflectance in VIS-NIR offers the highest signal-to-noise ratio of all Earth-viewed scenes because they are the brightest targets observed with near-overhead sun conditions in the tropics. They are also located at the tropopause level, where there is very little water vapor absorption above. The DCC calibration technique (DCCT) is a large-ensemble statistical approach that does not rely on any individual DCC cell. When observed collectively, DCC behave as an invariant target. The spatial distribution of DCC varies relative to sun position over the year. That is, the spatial and temporal distribution of DCC is a function of season, however, the inter-annual variability is very small. Because DCC are not fixed targets, the DCC sampling will have solar and view angular distributions that vary by season. For sun-synchronous orbits, these angular distributions will repeat annually. The DCC measurements in VIS-NIR spectrum are also the most Lambertian of all Earth targets and require only small bidirectional reflectance distribution function (BRDF) corrections. For VIS-NIR, the SNPP-VIIRS DCC monthly reflectance trend standard error (SE) was found to be 0.5% during the first two years of operation [8]. However, for some VIIRS SWIR bands, the trend SE exceeded 2%.

The VIS-NIR reflectivity of DCC is mainly a function of optical depth. For the SWIR bands, the reflectance is both a function of effective diameter and optical depth [9]. With an increase in the ice effective diameter, the single scattering albedo decreases, thereby increasing absorption, which in turn reduces the reflection back to space. However, the asymmetry factor increases with increasing particle size. The DCC SWIR reflectance is highly dependent on wavelength. For the VIIRS 1.6  $\mu\text{m}$  and 2.1  $\mu\text{m}$  bands, larger ice particles absorb more than smaller particles. This characteristic allows the 1.6  $\mu\text{m}$  reflectance to be compared with the 0.65- $\mu\text{m}$  reflectance for determining the particle size [9]. The 1.38- $\mu\text{m}$  channel is located in a strong water vapor absorption band, where any solar radiation is mostly absorbed by the underlying atmosphere, except in the case of high altitude clouds, thus making it an ideal channel for identifying ice clouds [10]. By comparing the 1.38  $\mu\text{m}$  reflectance to the neighboring 1.24  $\mu\text{m}$  window channel, the above cloud water vapor attenuation can be estimated. The DCCT will need to separate sensor calibration drifts and reflectivity variations due to optical depth, particle size, and above-cloud water vapor variations. As with the VIS-NIR bands, the DCC microphysics within in the DCC spatial and temporal distribution should be annually repeatable. Therefore, the key to the DCCT is seasonal characterization of the collective DCC reflectance.

The use of DCC reflectance as a means for post-launch calibration of satellite sensors was pioneered by Hu et al. [11], who used DCCT to evaluate the radiometric stability of TRMM VIRS and Terra MODIS imagers. Doelling et al. [12] found that for the Aqua-MODIS VIS-NIR channels,

the probability density function (PDF) mode is more suitable to evaluate the sensor stability than the mean, whereas for SWIR bands the mean is preferable. Wang and Cao [13] also confirmed using VIIRS observations that for VIS-NIR bands, the PDF mode is the statistic that provides the better stability analysis. Additionally, the DCC reflectance value depends on the 11  $\mu\text{m}$  brightness temperature (BT) threshold, season, and DCC core size, but has little effect on the overall stability. Mu et al. [14] varied the DCCT parameter thresholds in order to optimize the stability analysis as a function of MODIS wavelength. For bands with strong water vapor absorption (1.38  $\mu\text{m}$  and 0.94  $\mu\text{m}$ ), the BT threshold should be less than 205 K, whereas for all other bands the stability improves with increasing BT up to 205 K. The study found that the PDF bin size is insignificant. The visible (0.65  $\mu\text{m}$ ) and IR (11  $\mu\text{m}$ ) spatial homogeneity thresholds were already optimized by previous studies [8,12,14], which also recognized that the DCC reflectance seasonal cycle was greater in the SWIR bands than that for the VIS-NIR bands, and that the Hu DCC BRDF was effective only for the VIS-NIR bands. In summary, for SWIR bands, the DCCT is most sensitive to the BRDF, BT threshold, land/water surface type, and mode or mean PDF statistic, and produces a significant seasonal cycle of DCC reflectivity. These properties will be addressed in this study.

The key to improving the DCCT for SWIR bands is proper seasonal characterization of the DCC reflectance. Bhatt et al. [15] employed a deseasonalization technique to the MODIS DCC reflectance by subtracting the relative seasonal DCC reflectivity from the DCC reflectance values. However, at least two years of a sensor record is required for deseasonalization to be feasible. That is, the deseasonalization approach is not applicable in an initial calibration stability analysis soon after instrument launch. To detect SWIR channel calibration drift without a deseasonalization technique, a channel specific BRDF model approach is proposed. The BRDF model is constructed using the SNPP VIIRS five-year record and should be applicable to all sensors in the Aqua, SNPP, and JPSS orbit. This approach will enable a VIIRS SWIR band stability analysis on any future JPSS platform soon after launch, and will meet the CERES project SW flux stability requirement.

The paper is outlined as follows. The CERES VIIRS imager DCCT baseline method is described in Section 2. The baseline DCCT is analyzed for stability for both VIIRS VIS-NIR and SWIR bands, and is further analyzed with and without the Hu DCC BRDF model. Both all-season and monthly VIIRS DCC BRDF approaches are considered. The BRDF results are analyzed in Section 3. The VIIRS channel-specific BRDFs are tested with Aqua-MODIS—an instrument holding the same local equator crossing time orbit as VIIRS—band DCC reflectances to evaluate their applicability to future VIIRS sensors. The conclusions are presented in Section 4.

## 2. Methodology

First implemented by Hu et al. [11], the DCCT is a large-ensemble statistical approach that relies on the assumption that the distribution of DCC reflectance in the visible spectrum remains constant in time. Any observed shift embedded in the DCC reflectance distribution over time can then be attributed to satellite sensor degradation. The CERES project DCCT approach has been utilized as a pivotal method for vicarious calibration of numerous satellite sensors, including AVHRRs [16,17], MODIS [5,18,19], GEOs [20,21], and SNPP VIIRS [8,22]. In a recent study, Bhatt et al. [15] formulated a method of using DCC for characterizing the response vs. scan-angle (RVS) feature of the MODIS scan mirror in order to mitigate the scan-angle dependencies observed in the Aqua-MODIS calibration. The VIIRS and MODIS data sources are documented in the next section, followed by a brief description of the CERES VIIRS VIS-NIR DCCT baseline method and the construction of the DCC BRDF.

### 2.1. Data

The VIIRS data used in this study are a reformatted subset of the SNPP VIIRS V1 dataset generated by the NASA Land Product Evaluation and Analysis Tool Elements (PEATE) for support of independent cloud retrievals for the CERES project at the NASA Langley Research Center (LaRC). The subsetted VIIRS data contain reflectance data for 10 reflective solar bands (RSB), namely M3

(0.49  $\mu\text{m}$ ), M4 (0.55  $\mu\text{m}$ ), M5 (0.67  $\mu\text{m}$ ), M7 (0.86  $\mu\text{m}$ ), M8 (1.24  $\mu\text{m}$ ), M9 (1.38  $\mu\text{m}$ ), M10 (1.61  $\mu\text{m}$ ), M11 (2.25  $\mu\text{m}$ ), I1 (0.64  $\mu\text{m}$ ), and I3 (1.61  $\mu\text{m}$ ), which can be downloaded from the Atmospheric Science Data Center Distributed Active Archive Center (ASDC DAAC) at NASA LaRC. In a similar fashion, the Aqua-MODIS Collection 6 level 1B radiances are subsetted for the CERES project. For this study, Aqua-MODIS band 5 (1.24  $\mu\text{m}$ ), band 7 (2.12  $\mu\text{m}$ ) and band 26 (1.38  $\mu\text{m}$ ) are utilized. Both VIIRS (750-m nominal) and MODIS (1-km nominal resolution) level 1-B radiances are sub-sampled at every other scanline and pixel.

## 2.2. DCC Baseline Method

The CERES VIIRS VIS-NIR baseline DCCT is described in the global space based inter-calibration system (GSICS) algorithm theoretical basis document (ATBD) [23] and by Doelling et al. [12], who use globally acquired DCC pixels over the tropics ( $\pm 20^\circ$  latitude). A satellite imager pixel is identified as a valid DCC target if it meets all of the following criteria:  $BT$  (11  $\mu\text{m}$ )  $< 205$  K,  $\sigma_{\text{VIS}}$  (0.65  $\mu\text{m}$ )  $< 3\%$  and  $\sigma_{\text{BT}}$  (11  $\mu\text{m}$ )  $< 1.0$  K, where  $BT$  is the brightness temperature, and  $\sigma_{\text{VIS}}$  and  $\sigma_{\text{BT}}$  are the spatial standard deviations of a  $3 \times 3$  pixel block surrounding the designated pixel. These two spatial uniformity thresholds are helpful for capturing the DCC cores while filtering out any cloud edges or cloud tops with three-dimensional structure. Cloud top structure, e.g., overshooting convective tops, can cause shadows over lower parts of the cloud anvil and increase the anisotropic reflectance of the cloud. Solar zenith angles (SZAs) and viewing zenith angles (VZAs) are restricted to  $40^\circ$  to take advantage of the more Lambertian part of the DCC reflectance. The valid DCC pixels are normalized to a common set of angular conditions by way of an anisotropic correction based on the Hu DCC BRDF [11]. The anisotropic-corrected, or normalized, DCC pixel radiances are then compiled into monthly probability distribution functions (PDFs). The modes of the monthly PDFs, which provide peak frequencies of DCC reflectance, are tracked over time to monitor the temporal radiometric stability of the sensor.

Previous studies [5,8,13,15–17] have shown that the baseline DCCT offers a more robust time series of DCC response for VIS-NIR channels compared to any other Earth-view surface invariant target. However, because of the DCC particle-size-dependent absorption characteristics, the PDF mode is not necessarily stable for the SWIR bands. The baseline DCCT results in large seasonal cycles in the DCC time series for SWIR bands in VIIRS [8] and MODIS [12,14,15]. Figure 1 illustrates the seasonal PDF variability between the VIIRS VIS-NIR and SWIR bands. The VIS-NIR PDF peak frequency value is found to be a function of season (see Figure 1, left panel, where each line color represents a different month of the year), however, the PDF mode remains stable over time. For SWIR bands, the PDF structure is a function of season, where the PDF mode varies by season (see Figure 1 middle and right panels, where the blue lines represent August PDFs of multiple years). For SWIR bands, the PDF mean normalized radiance values have a smaller seasonal cycle than that for the PDF mode, which was confirmed by Doelling et al. [12]. The SWIR bands have more of a Gaussian DCC normalized radiance distribution than that for the VIS-NIR bands, which are negatively skewed. Mu et al. [14] also noted that the Hu DCC BRDF, which was designed for VIS-NIR bands, was inadequate for SWIR bands. Although these previous studies have evaluated the stability effectiveness of the DCCT PDF mode and mean and the Hu DCC BRDF, we perform the DCCT method as a function of PDF statistic, with and without Hu DCC BRDF for both VIS-NIR and SWIR bands as a reference. These assessments are done as a means to evaluate improvements to the DCCT. The temporal SE of regression is chosen as a key parameter for improvement evaluation, as it is directly associated with the minimum detectable trend magnitude for a given DCC time series [8]. Only trends that exceed the natural variability (or seasonal cycles) of the time series can be detected with statistical significance. Therefore, lowering the SE in the DCC time series always enhances the detectability of the satellite sensor radiometric trend at small magnitudes.

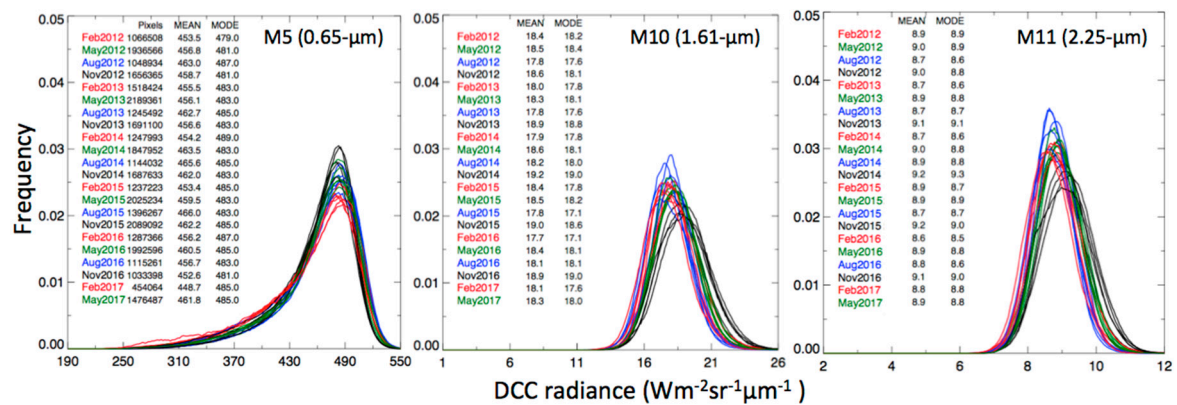
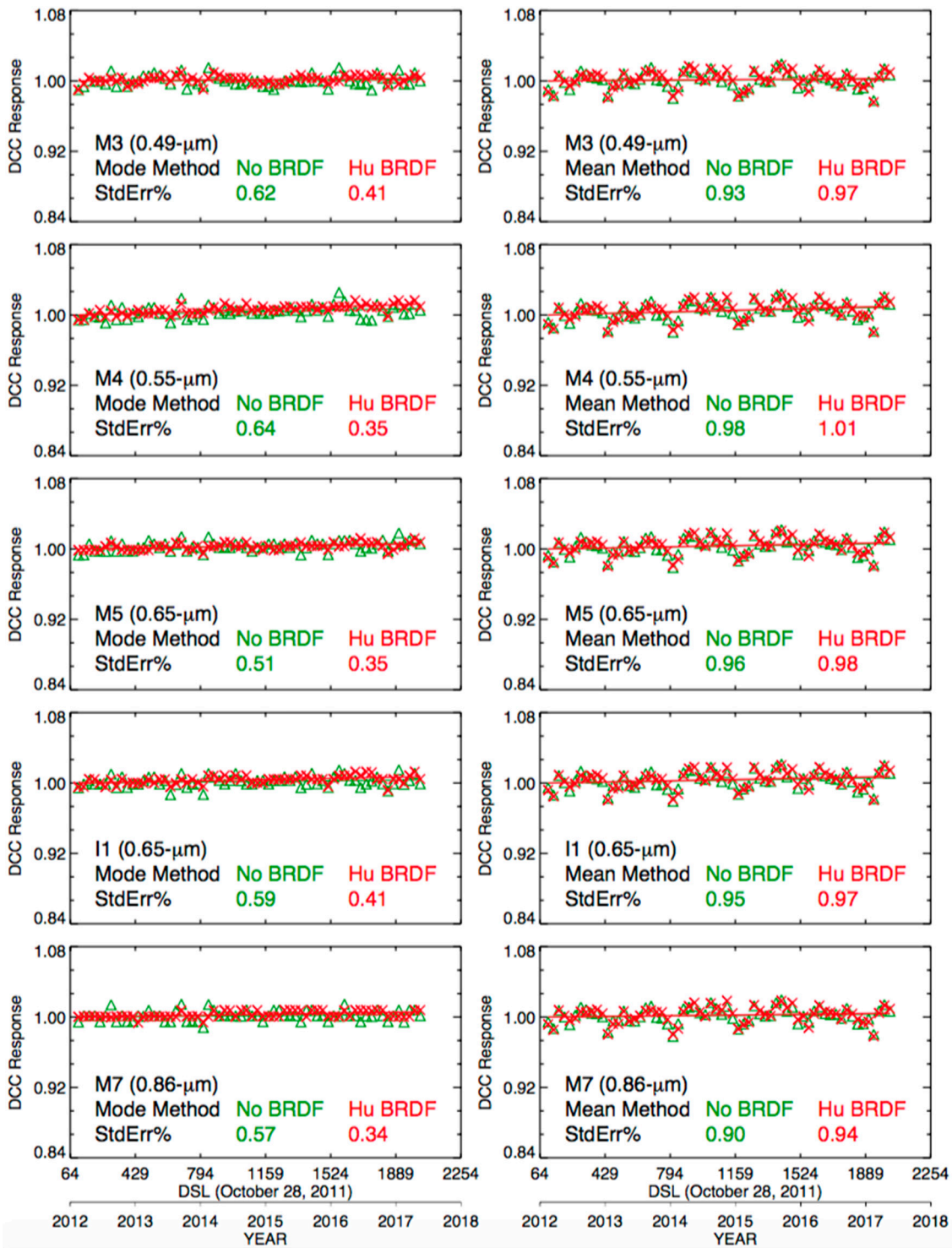


**Figure 1.** Monthly deep convective clouds (DCC) probability density function (PDF) radiance plots for the VIIRS: M5 band (left panel); M10 band (middle panel); and M11 band (right panel). The monthly number of DCC identified pixels, the PDF mean, and PDF mode DCC normalized radiance values are also listed.

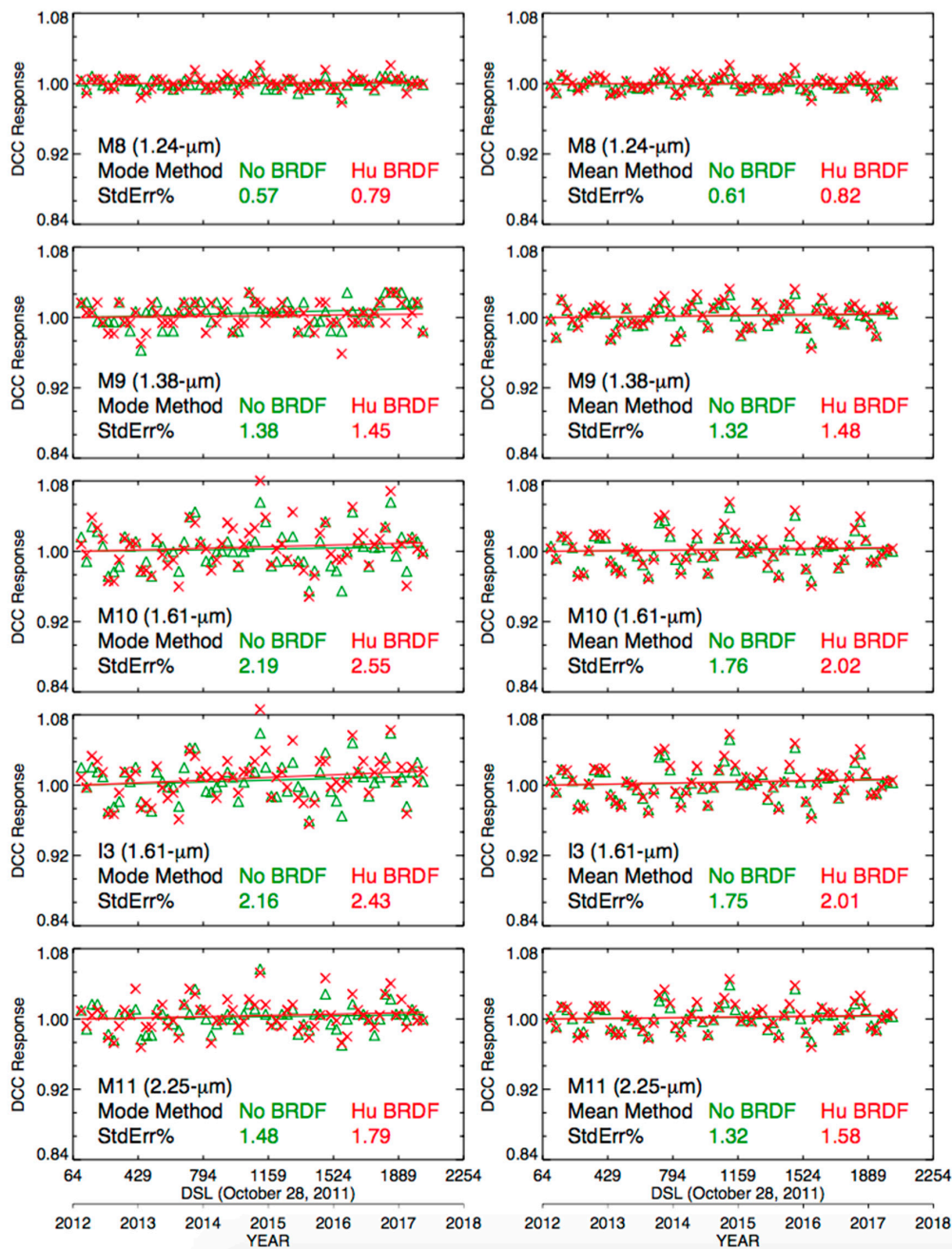
### 2.3. Hu DCC BRDF

Figure 2 shows the DCC monthly mode and monthly mean time series for SNPP-VIIRS VIS-NIR, with and without the use of Hu BRDF for anisotropic corrections. The time axis is provided in both days since launch (DSL) and year units. The time series data are normalized to 1 at the beginning of the record. It is evident in Figure 2 that the application of Hu BRDF for VIS-NIR bands results in reduction of the temporal standard error by one-third. Using the PDF mode rather than the mean also reduces the temporal standard error by one-third (no BRDF correction). Incorporating both the Hu BRDF and the PDF mode reduces the standard error by two-thirds. The Hu BRDF is ineffective when applied to the PDF mean.

For SWIR bands (Figure 3), the DCC normalized response exhibits large seasonal cycles in both the mode and mean time series. For VIIRS bands M8 and M9, the PDF mean and mode standard errors are similar. For the VIIRS M10, M11, and I3 bands, the PDF mean has 20% less temporal variability than the PDF mode (no BRDF). This pattern substantiates the findings of Doelling et al. [12], in that the PDF mean is preferable for SWIR bands. The Hu BRDF model increases the monthly DCC response variability by 35% and 5% for the M8 and M9 bands, respectively, and by ~15% in the M10, M11 and I3 bands. The results confirm the Mu et al. [14] conclusion that the Hu DCC BRDF is inadequate. We propose a channel-specific SWIR DCC BRDF that is aimed to account for the seasonal variation of the DCC response.



**Figure 2.** The normalized DCC Mode (left); and Mean (right) reflectance time series with (red “×”) and without (green “Δ”) Hu anisotropic corrections for VIIRS VIS and NIR bands, with corresponding linear trend line and standard error in percent.



**Figure 3.** The normalized DCC Mode (**left**); and Mean (**right**) reflectance time series with (**red “x”**) and without (**green “Δ”**) Hu anisotropic corrections for VIIRS SWIR bands, with corresponding linear trend line and standard error in percent.

#### 2.4. Channel Specific All-Season DCC BRDF

Empirical SWIR channel-specific DCC BRDF models are constructed by partitioning the DCC-identified pixel-level reflectances into angular bins as described in Suttles et al. [24], and Loeb et al. [25]. For this study, a dense set of DCC reflectance data acquired from the first five years of VIIRS RSB measurements during 2012–2017 is used to compute the BRDF models. DCC pixels are selected globally near the tropics ( $\pm 20^\circ$  latitude) using the same DCC identification thresholds as described in the DCC baseline method (Section 2.2), except that the SZA and VZA thresholds are extended to  $55^\circ$ . The DCC reflectance is characterized as a function of VZA, SZA, and relative azimuth angle (RAA). The VZA and SZA are discretized into 11 bins ( $5^\circ$  step size) ranging from  $0^\circ$  to  $55^\circ$ ,

whereas the binning of RAA is performed at  $10^\circ$  intervals (18 bins) varying from  $0^\circ$  to  $180^\circ$ . This results in a total of  $11 \times 11 \times 18 = 2178$  angular bins for each band. The DCC pixel-level reflectances acquired in each bin are recorded along with their mean and standard deviation. For each SZA bin, the albedo is computed by integrating the DCC reflectances by the solid angle defined by the VZA and RAA bin, as described in [24]. This computed albedo is not the true albedo because only the sampled satellite sensor bins are used in the computation. The BRDF factor ( $\chi$ ) is the bin reflectance divided by the corresponding albedo. Positive  $\chi$  indicate that the reflectance is greater than the overall albedo.

Figure 4 shows the polar plots of the derived  $\chi$  values for the SZA of  $22.5^\circ$ . Each polar plot represents  $\chi$  values for an individual VIIRS band. The bin observed DCC reflectance is simply the albedo multiplied by  $\chi$ . The channel specific DCC  $\chi$  values for the VIIRS VIS-NIR bands (M3, M4, M5 and M7) indicate that the anisotropic correction factors are similar for wavelengths less than  $1 \mu\text{m}$ . This result justifies the application of the same Hu model to all of the VIS and NIR bands DCC measurements.

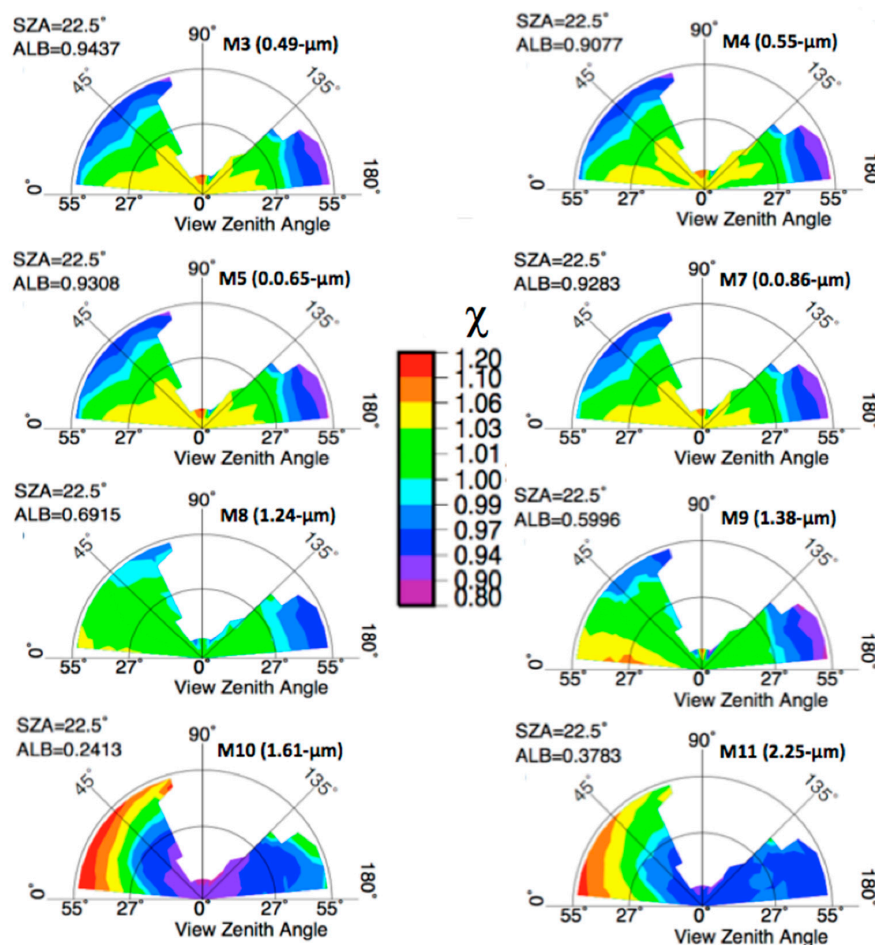


**Figure 4.** The annual BRDFs of the VIIRS RSB reflectances for the  $5^\circ$  SZA bin centered at  $22.5^\circ$ . The radial coordinate represents VZA (range  $0^\circ$  to  $55^\circ$ ) with a  $5^\circ$  bin size, whereas the angular coordinate represents RAA with a  $10^\circ$  bin size. Direct forward scatter has an RAA of  $0^\circ$ , whereas a direct backscatter has an RAA of  $180^\circ$ . The white spaces are un-sampled bins.

For VIS-NIR bands, the DCC albedos are very bright and the BRDF patterns are similar with greatest reflectances observed near nadir conditions. However, the DCC BRDF and albedos are unique for each of the SWIR bands. For wavelengths greater than  $1.6 \mu\text{m}$  (M10 and M11), the lowest DCC reflectances are found near nadir. The M10 and M11 bands have increased DCC reflectance for larger VZA in the forward-scattering direction. In addition, the M10 and M11 DCC reflectance values are

quite dark due to the DCC ice particle absorption properties. The M8 channel is found to be the most Lambertian band, with DCC reflectance slightly higher than that of M9 channel, which contains a water vapor absorption band. Both the M8 and M9 bands also reveal a slight increase in DCC reflectance in the forward-scattering direction.

The observed DCC reflectance ( $\rho$ ) is corrected for anisotropy by normalizing to a single set of angular condition using the following equation:

$$\rho_{\text{corrected}} = \rho_{\text{observed}} [\text{BRDF}(22.5^\circ, 32.5^\circ, 145^\circ) / \text{BRDF}(\text{SZA}, \text{VZA}, \text{RAA})] \quad (1)$$

For this study, the angular condition chosen for normalization is  $\text{SZA} = 22.5^\circ$ ,  $\text{VZA} = 32.5^\circ$ , and  $\text{RAA} = 145^\circ$ . The chosen angular condition corresponds to the angular bins with highest number of DCC samples acquired by VIIRS and does not impact the relative corrected DCC reflectance, however, it will determine DCC reflectance magnitude.

### 2.5. Channel-Specific Monthly DCC BRDF

The spatial location of DCC and the associated polar orbital angular sampling patterns of DCC tend to repeat annually. For VIS-NIR bands, the reflective properties of DCC are mostly based on the optical depth [9]. The spatial standard deviation of the 0.65- $\mu\text{m}$  MODIS annual regional ( $10^\circ$  latitude by  $10^\circ$  longitude) DCC reflectance was found to be  $\sim 0.6\%$  (Table 5, tropics, 205 K, mode of [12]). However, for SWIR bands, both the optical depth and the particle size determine the DCC reflectance. The standard deviation of the 1.37- $\mu\text{m}$  and 2.12- $\mu\text{m}$  MODIS regional DCC reflectance was 2.8% and 2.0%, respectively [12]. The polar orbiter angular sampling pattern varies monthly due to the solar declination angle, which influences the spatial distribution of the DCC. For the all-season DCC BRDF, some of the angular bins could be sampled from multiple months of the year. Thus, the all-season DCC BRDF would dampen out these DCC reflectance seasonal cycles, thereby increasing the seasonal noise in the DCCT. A monthly DCC BRDF should be able to characterize the regional DCC reflectance seasonal cycles. This assumption can be tested by comparing the resulting trend standard errors for both the all-season and monthly DCC BRDFs. The BRDF model deseasonalization effectiveness can be assessed by deseasonalizing the monthly BRDF-corrected DCC reflectance response. If the trend standard errors between response with and without deseasonalization are similar, then the BRDF model is extremely effective in characterizing the DCC reflectance seasonal cycles.

The channel-specific DCC BRDF models are constructed by further subsetting the DCC reflectances into monthly bins. A monthly decomposition of the all-season DCC BRDF reflectance for the VIIRS M11 (2.25  $\mu\text{m}$ ) SWIR band is shown in Figure 5 for January, April, July, and October. The same SZA of  $22.5^\circ$  is chosen to facilitate comparison with Figure 4. It is worth mentioning that the VZA and AZA angular distribution is the same for each of the five occurrences of January during 2012–2016 in the SNPP VIIRS dataset (not shown). However, the month-to-month angular distribution does change, which is due to orbital sampling and the spatial location of the tropical DCC. Figure 5 shows that the DCC reflectance is similar for matched angular bins for January, April, and July. In October, the average bin reflectance is larger than that of the other months. The VIIRS 1.61  $\mu\text{m}$  (not shown) and 2.25  $\mu\text{m}$  bands exhibit the largest seasonal DCC BRDF dependencies.

The seasonal variability in the SWIR DCC response was demonstrated in Figure 1, where the monthly PDFs are shifted along the radiance axis for certain months of the year. This pattern suggests that applying an all-season BRDF is inadequate to account for the observed month-to-month variation in the SWIR DCC response that was also shown in Figure 5. Figure 1 also predicts that the DCC BRDF structure for the VIIRS M5 (0.65  $\mu\text{m}$ ) band should be similar for all months. This idea is illustrated in Figure 6, where the M5 DCC reflectances are very similar for all four months. It must be noted that the reflectance scales are different for Figures 5 and 6. A 0.01 increment in DCC reflectance in Figure 6 represents a 1.1% relative change, whereas in Figure 5, a 0.01 increment represents a 2.6% relative change.

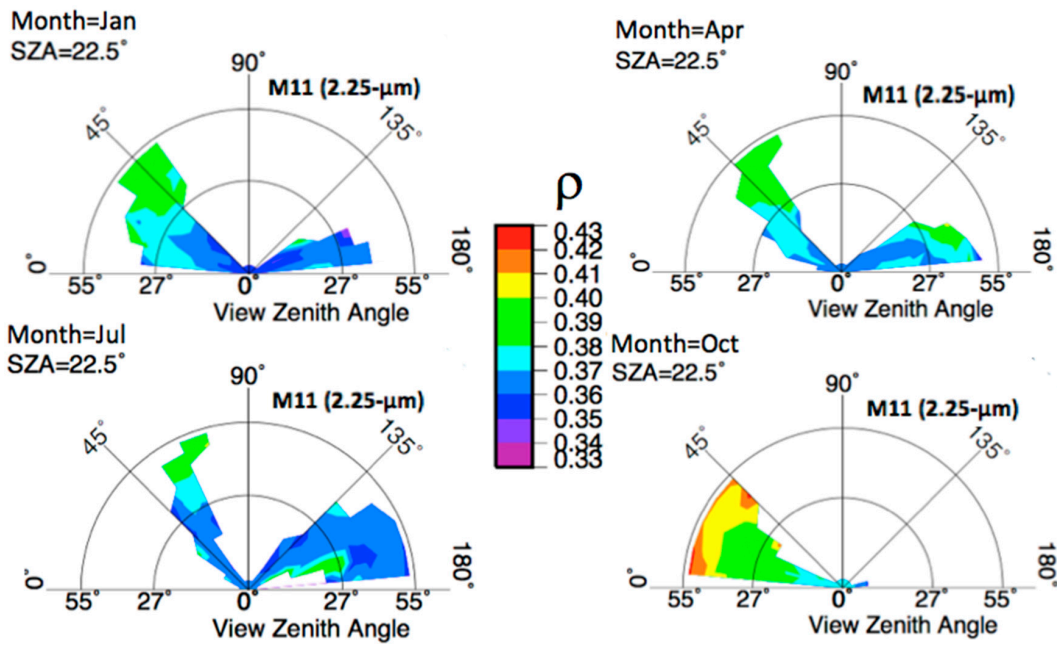


**Figure 5.** The January, April, July and October DCC reflectances of the VIIRS M11 (2.25 μm) shortwave infrared (SWIR) band reflectances for the 5° SZA bin centered at 22.5°. The VZAs (range 0° to 55°) are shown along the radial coordinate with a 5° bin size, and RAAs are shown on the angular coordinate with a 10° bin size. Forward scattering is found at RAA = 0.

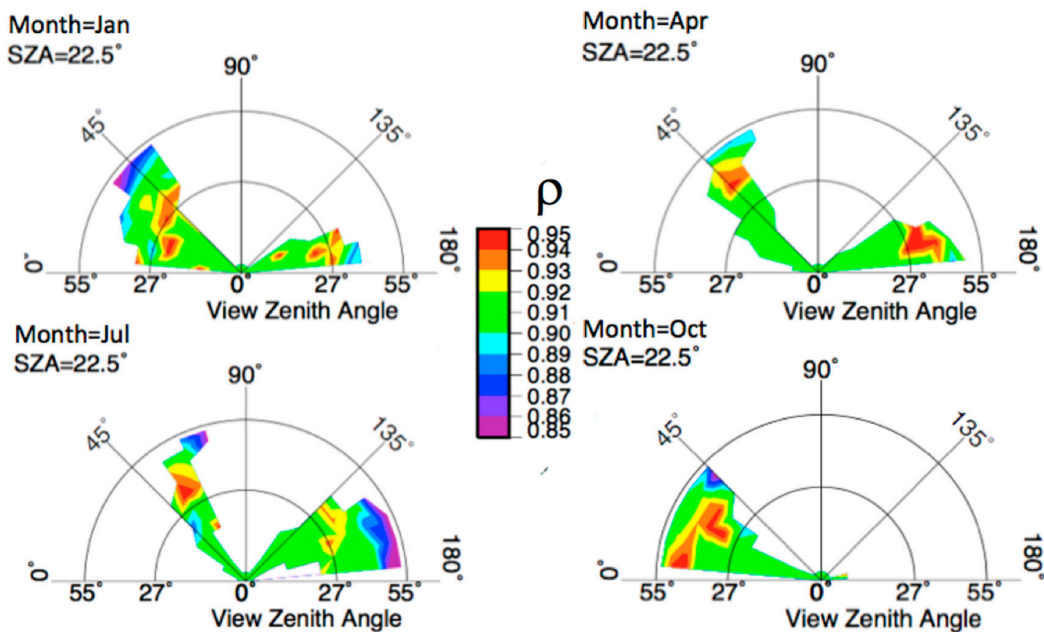


**Figure 6.** The January, April, July and October DCC reflectances of the VIIRS M5 (0.65 μm) VIS band reflectances for the 5° SZA bin centered at 22.5°. The VZAs (range 0° to 55°) are shown along the radial coordinate with a 5° bin size, and RAAs are shown on the angular coordinate with a 10° bin size. Forward scattering is found at RAA = 0.

For the monthly BRDF, the DCC pixel reflectance is first adjusted for anisotropy using a month-specific BRDF factor, and then normalized to the same arbitrary angular condition as the

all-season BRDF model. A BRDF-corrected DCC reflectance pixel is thus derived using the following equation:

$$\rho_{\text{corrected}} = \rho_{\text{observed}} [\text{BRDF}(22.5^\circ, 32.5^\circ, 145^\circ) / \text{BRDF}(\text{SZA}, \text{VZA}, \text{RAA}, \text{Month})]. \quad (2)$$

### 2.6. Deseasonalization

The effectiveness of the VIIRS-based DCC BRDFs in mitigating the SWIR band month-to-month DCC response variability is evaluated against the direct deseasonalization of the non-anisotropic corrected DCC response time series. The deseasonalization is performed using a ratio-to-moving average method as outlined by Bhatt et al. in [15]. A relative ratio is computed for each monthly DCC reflectance, and then divided by the 12-month running mean centered on the given month. The individual observed month DCC reflectance is then divided by relative ratio for the observed month. This multi-step technique is more robust than simply averaging all of the yearly DCC reflectances for a given month and subtracting the value from the observed monthly value—a method intended for timelines with no apparent trend or drift. The ratio-to-moving average leaves intact any drift in the time series. The ratio-to-moving average deseasonalization method requires at least two complete years of data to compute monthly relative ratios for 12 months. The longer is the record used to create the relative ratios, the greater is the mitigation of the seasonal cycle, all while still preserving the embedded sensor calibration drift.

## 3. Results and Discussion

The VIIRS-based all-season and monthly DCC BRDF models for SWIR bands are evaluated in this section. The effectiveness of the monthly BRDF in reducing temporal variation compared to using an all-season BRDF for each spectral band is assessed. Furthermore, the applicability of these monthly BRDF models to future imagers with similar spectral channels and satellite orbit characteristics is examined by applying them to the corresponding SWIR bands of Aqua-MODIS. Because the orbital characteristics of Aqua-MODIS resemble that of SNPP VIIRS, they both should sample the same angular conditions relative to DCC.

### 3.1. BT Threshold DCC Reflectance Sensitivity

For MODIS, the IR calibration is stable over time to within 0.1 K when compared to the Atmospheric Infrared Sounder (AIRS) [26]. Similarly, for VIIRS, the IR calibration is within 0.1 K of the Infrared Atmospheric Sounding Interferometer (IASI) [27]. The DCC reflectivity has been noted to be dependent on the BT threshold. That is, in order to determine the change in DCC reflectivity as a function of the BT threshold, the BT threshold was varied between 196 K and 205 K and the DCC reflectance difference was noted (Figure 7 as drift percent). The DCC reflectance drift as a function of temperature is mostly linear. For M5 (0.65  $\mu\text{m}$ ) the DCC reflectance increases by 0.15% (0.42%) for every 1-K decrease in terms of the mode (mean) PDF statistic. The DCC reflectance sensitivity owed to the BT threshold DCC reflectance sensitivity is one-third less for the PDF mode than that for the mean. This result is another reason why the PDF mode is the preferred PDF statistic for VIS-NIR bands. For the M11 (2.25  $\mu\text{m}$ ) band, the DCC reflectance increases by 0.59% (0.51%) for every 1-K decrease in terms of the PDF mode (mean) method. For the M11 band, the BT threshold is similar for either PDF mode or mean statistics. Given that the MODIS or VIIRS IR calibration stability is within 0.1 K, the M11 band DCC reflectivity sensitivity with respect to the BT threshold is predicted to be within  $\sim 0.05\%$ , which is insignificant compared to other uncertainty sources of the DCCT.

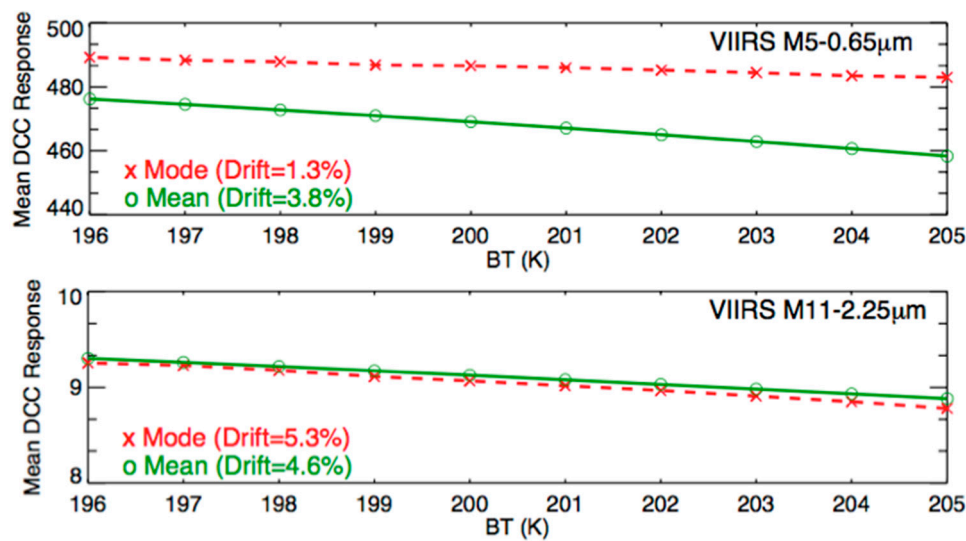


**Figure 7.** The VIIRS M5 (0.65  $\mu\text{m}$ ) (**top panel**); and M11 (2.25  $\mu\text{m}$ ) (**bottom panel**) DCC normalized radiance as a function of BT (11  $\mu\text{m}$ ) threshold. The drift is the change in DCC radiance in percent between 196 K and 205 K. The dashed and solid lines shown above simply connect the adjacent data points.

### 3.2. Comparison of the All-Seasonal and Monthly DCC BRDF

The comparison between the resulting DCC reflectance time series using monthly and all-season BRDF corrections is shown in Figure 8. These results can be compared with the uncorrected version (no BRDF correction) shown in Figure 3 (green points on right panel). The DCC reflectance standard error (SE) statistics are compiled in Table 1. For VIIRS bands M10, M11, and I3, the SE is reduced by ~40% using all-season BRDF models with respect to that for no BRDF correction. The improvements in bands M8 and M9 are ~15% and 5%, respectively, when using the all-season BRDF. The performance of the monthly DCC BRDF models is superior to that of the all-season BRDF corrections. The temporal variation in the monthly DCC response is significantly reduced, by ~55%, in bands M10, M11, and I3, and by ~42% in bands M8 and M9 after applying monthly BRDF models compared to that for no BRDF correction. All VIIRS SWIR bands that use the monthly BRDFs have trend SE within 0.8%. Clearly, the monthly BRDFs remove more of the seasonal signature of the DCC reflectance than the all-season BRDF. One would also expect the PDF shapes to be similar over the 12 months relative to without application of the monthly BRDF model. A new set of monthly PDFs is derived for VIIRS M10 and M11 bands after applying the monthly BRDF models. These results are shown in Figure 9. Compared to the no BRDF PDF plots (Figure 1), the new PDFs for M10 and M11 bands exhibit consistent shapes and more stable PDF modes, signifying that the monthly BRDFs have mitigated most of the seasonal variance in the SWIR bands DCC response.

By comparing the uncorrected (no BRDF correction) with the deseasonalized uncorrected results, the seasonal contribution of the DCC reflectivity variations can be estimated. Table 1 reveals that, for SWIR bands, the seasonal contribution of the DCC reflectance variation is up to ~50%. In order for the DCC BRDFs to be successful, the SE must be less than that for the deseasonalized uncorrected case. Only the monthly BRDF has smaller SEs than that for the deseasonalized uncorrected case. To determine the deseasonalization efficiency of the DCC BRDF model, the SE results for cases with and without deseasonalized BRDF are compared. Deseasonalization reduced the monthly BRDF SE by 10%, revealing that the monthly BRDF model has ~90% deseasonalization efficiency, whereas the all-season case has a 55% to 70% deseasonalization efficiency depending on the SWIR band. After deseasonalization, both the all-season and monthly BRDFs have similar SEs. For all SWIR bands, using both monthly BRDF and deseasonalization provides the lowest DCC reflectance SEs.

As mentioned previously, however, the deseasonalization option is only available after two years of observations.

**Table 1.** Comparison of temporal standard error in percent for VIIRS SWIR bands using no, all-season, and monthly DCC BRDF corrections for tropical ocean and land. The standard errors in parenthesis are after deseasonalization.

VIIRS Band Ocean and Land	No BRDF	All-Season BRDF	Monthly BRDF
M8 (1.24 $\mu\text{m}$ )	0.61 (0.35)	0.51 (0.31)	0.34 (0.30)
M9 (1.38 $\mu\text{m}$ )	1.32 (0.75)	1.24 (0.70)	0.77 (0.70)
M10 (1.61 $\mu\text{m}$ )	1.76 (0.90)	1.05 (0.72)	0.78 (0.69)
I3 (1.61 $\mu\text{m}$ )	1.75 (0.93)	1.06 (0.75)	0.81(0.72)
M11 (2.25 $\mu\text{m}$ )	1.32 (0.67)	0.83 (0.55)	0.60 (0.53)

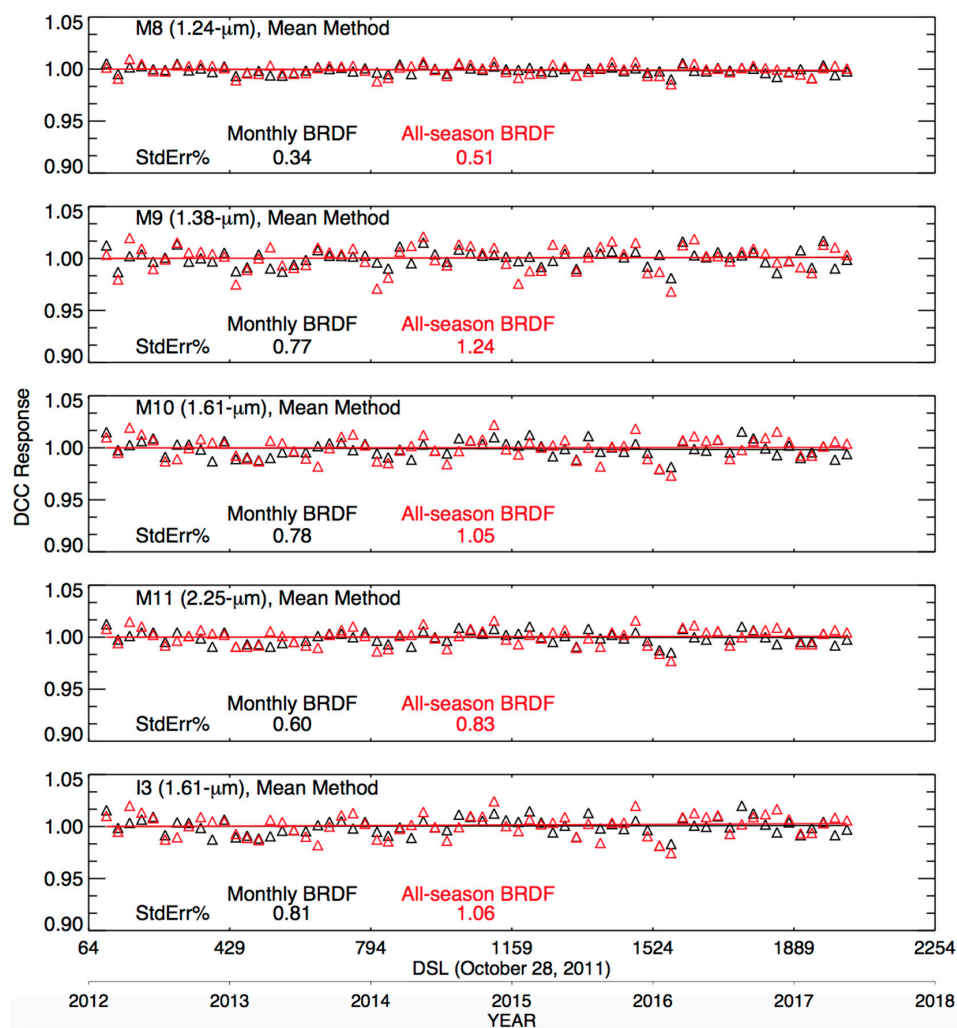


**Figure 8.** The normalized DCC Mean reflectance time series with either all-season (red) or monthly (black) DCC BRDF anisotropic corrections for VIIRS SWIR bands with corresponding linear trend lines and standard error in percent.

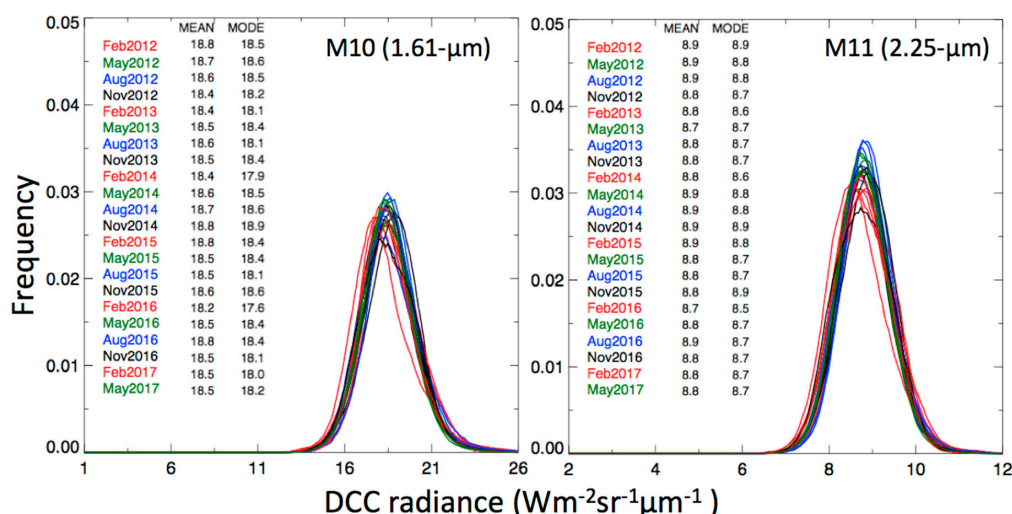


**Figure 9.** Monthly DCC PDF radiance plots for the VIIRS M10 and M11 bands after applying monthly BRDF corrections to individual DCC pixels. Compare to Figure 1.

### 3.3. Ocean and Land BRDF Analysis

Table 1 contains the BRDF SEs based on all tropical surface types. Doelling et al. [12] found that for MODIS SWIR bands the land DCC was more stable than that over ocean. To determine the deseasonalization potential between ocean, land, and ocean and land combined, the uncorrected (no BRDF correction) trend SEs are computed for these three surface options. The same is done for the corresponding deseasonalized uncorrected trend SEs. The ocean and land, ocean-only, and land-only statistics are shown in Table 2. The uncorrected SE was smallest for ocean-only, with the exception of the M9 band. For the VIIRS SWIR bands, the land-only uncorrected SE was ~20% greater than that for ocean-only, again with the exception of the M9 band. The deseasonalized uncorrected SE for both ocean and land was similar to, or outperformed, the ocean-only or land-only surface type. To truly verify whether land-only or ocean-only has more predictable DCC reflective seasonal cycles, monthly BRDFs for land-only and ocean-only cases would need to be constructed. The construction of BRDF models is arduous and was not deemed worthwhile given the fact that ocean-only and land-only deseasonalization did not reduce the SE over both ocean and land. Previous studies [12,14] found that that the greatest occurrence of DCC is found in the tropical western pacific (TWP). Hong et al. [28] also confirms that the ice cloud frequency for the Aqua orbit is greatest over the TWP. Because the DCCT is a large-ensemble approach that requires sufficient sampling spatially, as well as regularly from all months over the year, the lack of sampling over a few months of the year can increase the DCC reflectance seasonal noise. Therefore, the preferred surface type for DCCT is the combined ocean and land condition.

**Table 2.** Comparison of temporal standard error in percent for VIIRS SWIR bands using the no BRDF correction for tropical ocean and land, ocean-only, and land-only. The standard errors in parenthesis are after deseasonalization.

VIIRS Band No BRDF	Ocean and Land	Ocean Only	Land Only
M8 (1.24 μm)	0.61 (0.35)	0.56 (0.36)	0.66 (0.40)
M9 (1.38 μm)	1.32 (0.75)	1.35 (0.82)	1.31 (0.80)
M10 (1.61 μm)	1.76 (0.90)	1.63 (0.90)	2.03 (1.16)
I3 (1.61 μm)	1.75 (0.93)	1.62 (0.93)	2.07(1.19)
M11 (2.25 μm)	1.32 (0.67)	1.19 (0.67)	1.54 (0.86)

### 3.4. Evaluation of VIIRS DCC BRDFs Using Aqua MODIS

To demonstrate that the SNPP-VIIRS DCC BRDF is valid for another sensor in the same orbit, the VIIRS BRDF is applied to Aqua MODIS. Both VIIRS and Aqua-MODIS satellites are in a 13:30 sun-synchronous orbit. The Aqua orbit has an altitude of 700 km and a period of 99 min, whereas the SNPP has an altitude of 830 km and a period of 101 min. The two orbits have consistent local time sampling of the DCC cycle, thereby avoiding any diurnal sampling differences of DCC properties. This is important because the mean onset and peak of convection is a function of local time. The VIIRS-based monthly DCC BRDFs are applied to the matching Aqua-MODIS SWIR bands. Similarly, an Aqua-MODIS DCC monthly BRDF is constructed in the same manner as VIIRS using the Aqua-MODIS DCC reflectances computed during 2002–2017. The two sets of BRDFs for Aqua-MODIS B5 (1.24  $\mu\text{m}$ ) and VIIRS M8 (1.24  $\mu\text{m}$ ), MODIS B26 (1.38  $\mu\text{m}$ ) and VIIRS M9 (1.38  $\mu\text{m}$ ), and MODIS B7 (2.12  $\mu\text{m}$ ) and VIIRS M11 (2.25  $\mu\text{m}$ ) bands are compared. The MODIS and VIIRS band spectral response functions are similar, except for the MODIS B7 and VIIRS M11 bands. Aqua-MODIS B6 (1.60  $\mu\text{m}$ ) is excluded in this assessment because more than half of its detectors are inoperable.

Figure 10 shows the DCC time series computed for the Aqua-MODIS SWIR bands using the PDF mean. For each band, the DCC reflectance time series is computed for four cases: (1) no BRDF (uncorrected); (2) Hu BRDF; (3) SNPP-VIIRS monthly BRDF; and (4) Aqua-MODIS monthly BRDF. As expected, the Hu BRDF adds more noise to the mean DCC time series for the Aqua-MODIS SWIR bands. The Aqua-MODIS uncorrected SE for B5 and B26 is slightly greater than its VIIRS counterpart, likely due to the fact that Aqua-MODIS is more susceptible to issues that arise from aging hardware. The performance of the VIIRS and MODIS-based monthly BRDF models are comparable (VIIRS being slightly better) for B5 and B26, as both result in the reduction of natural variability in the monthly DCC response by ~45%. MODIS B7 has the greatest uncorrected SE (2.85%) of all SWIR bands examined in this study. The neighboring VIIRS M11 band has an SE of 1.32%. Because of the spectral dissimilarities between M11 and B7, the VIIRS-based monthly BRDF is not applicable to MODIS B7. The MODIS-based monthly BRDF reduced the SE of the B7 DCC time series from 2.85% using no BRDF to 1.03%, a 64% reduction. For all SWIR bands, the major component of the SE is mainly owed to the large seasonal cycles that are repeated annually. The MODIS B7 and VIIRS M11 SE differences highlight the importance of a wavelength-specific BRDF when employing the DCCT for SWIR bands.

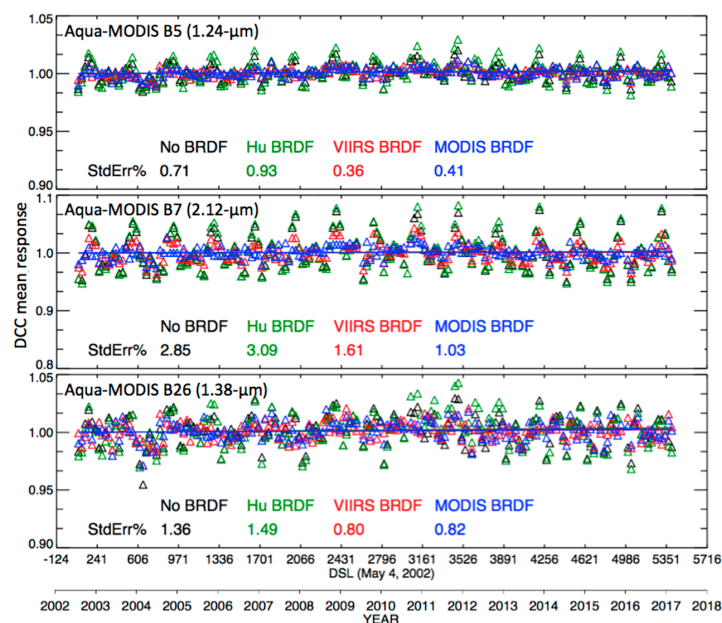


**Figure 10.** The normalized DCC Mean reflectance time series for Aqua-MODIS SWIR bands when using no BRDF, Hu BRDF, monthly VIIRS BRDF, and monthly MODIS BRDF.

#### 4. Conclusions

The DCC calibration technique (DCCT) is a large-ensemble statistical approach and does not rely on any individual DCC cell. When DCC are observed collectively, they behave as an invariant target. The success of DCCT for SWIR bands is based on the assumption that the spatial and temporal distribution of DCC reflectance varies by season, but the inter-annual variability is very small. The VIS-NIR band DCC reflectance is mainly a function of optical depth, however, for the SWIR bands, the DCC reflectance is also a function of particle size, which is more variable spectrally, temporally and geographically. It was shown that for the SWIR bands the DCC response SE (without BRDF) has a seasonal contribution of up to ~50%. Deseasonalization was found to be the most effective component of the DCCT for reducing the SE. However, deseasonalization requires at least two years of record to be viable.

This study analyzed the feasibility of BRDFs to mitigate the DCC response SE. It was assumed that the BRDF constructed from an imager in the same sun-synchronous orbit could be applied to another imager in the same orbit. It was demonstrated that the monthly DCC BRDF either outperformed or performed comparable to deseasonalization for all the SNPP VIIRS SWIR bands. The monthly DCC BRDFs had a 90% efficiency of mitigating the DCC response SE, indicating that, if deseasonalization were applied to the monthly BRDF-corrected DCC response, the SE would be reduced by another 10%. Before deseasonalization, the monthly BRDF-corrected DCC response SE was within 0.81% for all VIIRS SWIR bands, whereas, after deseasonalization, it was within 0.72%.

The feasibility of applying a DCC BRDF to a similar (in orbit) sun-synchronous imager was tested by constructing an SNPP-VIIRS DCC BRDF and applying it to the corresponding Aqua-MODIS SWIR bands. It was confirmed that the VIIRS BRDF provided the same MODIS DCC response SE as a MODIS BRDF would. However, the spectral bands must match closely because the DCC reflectance is a spectrally dependent, as was the case for comparing the VIIRS M11 (2.25  $\mu\text{m}$ ) and the MODIS B7 (2.12  $\mu\text{m}$ ) SWIR bands. It is anticipated that the SNPP-VIIRS and the four JPSS follow-on VIIRS imagers will have similar band spectral response functions.

This analysis also confirmed previous studies, in that for SWIR bands, the PDF mean statistic is preferred over the PDF mode and that the Hu BRDF model, which was developed specifically for VIS band, is ineffective. This study illustrates that the PDF mean DCC response (without BRDF) decreased the SE by 20% relative to the PDF mode statistic for SWIR bands, and that the Hu DCC BRDF increased the SE by 5 to 35%, depending on the VIIRS SWIR band. Previous studies suggest that the DCC reflectance for SWIR bands is a function of BT threshold. This study found that decrements of 1 K in the BT threshold corresponded to increments of 0.51% in the M11 (2.25  $\mu\text{m}$ ) band DCC reflectance. Since the predicted VIIRS or MODIS IR stability is 0.1 K, the DCC reflectance change is insignificant. Doelling et al. [12] suggests that land regions DCC reflectances are more predictable in the SWIR bands. This study notes that for certain SWIR bands, the DCC response (without BRDF) is more stable for land-only or ocean-only than for land and ocean combined. However, after deseasonalization, no advantage was found using either ocean-only or land-only. It is hypothesized that because the DCCT is a large-ensemble approach, it is more important for all months to be well sampled, rather than relying on very predictable regional diurnal DCC cycles, which may not be present throughout the year.

The monthly DCC BRDF approach should meet the CERES SW flux stability requirement for climate accuracy by mitigating any VIIRS imager SWIR band calibration drifts in all VIIRS sensors onboard the follow-on JPSS satellites.

**Acknowledgments:** The authors would like to thank the MODIS and VIIRS Characterization Support Team for their insights regarding the MODIS and VIIRS instruments. The SNPP-VIIRS and Aqua-MODIS sub-setted level1B files were obtained at the NASA-Langley Atmospheric Science Data Center Distributed Active Archive Center (ASDC DAAC). This work was supported by the National Aeronautics and Space Administration Earth (NASA) Science Enterprise Office through the CERES and Research Announcement (NRA) NNN15ZDA001N, Research Opportunities in Space and Earth Science (ROSES-2015), Program Element A.34: Satellite Calibration Interconsistency Studies.

**Author Contributions:** Rajendra Bhatt and David R. Doelling formulated the method of constructing the seasonal DCC BRDFs, analyzed the results and prepared the manuscript. Benjamin Scarino, Conor Haney, and Arun Gopalan helped with developing the VIIRS HDF file reader, processing the data, and reviewing the manuscript.

**Conflicts of Interest:** The authors declare no conflict of interest.

## References

1. Joint Polar Satellite System. Available online: [http://www.jpss.noaa.gov/mission\\_and\\_instruments.html](http://www.jpss.noaa.gov/mission_and_instruments.html) (accessed on 24 August 2017).
2. WMO OSCAR. Available online: <https://www.wmo-sat.info/oscar/satellites/view/342> (accessed on 24 August 2017).
3. Klaes, K.D.; Cohen, M.; Buhler, Y.; Schlüssel, P.; Munro, R.; Engeln, A.; Clérigh, E.; Bonekamp, H.; Ackermann, J.; Schmetz, J.; et al. An Introduction to the EUMETSAT Polar system. *Bull. Am. Meteorol. Soc.* **2007**, *88*, 1085–1096. [[CrossRef](#)]
4. Wielicki, B.A.; Barkstrom, B.R.; Harrison, E.F.; Lee, R.B., III; Smith, G.L.; Cooper, J.E. Clouds and the earth's radiant energy system (CERES): An earth observing system experiment. *Bull. Am. Meteorol. Soc.* **1996**, *77*, 853–868. [[CrossRef](#)]
5. Wu, A.; Xiong, X.; Doelling, D.R.; Morstad, D.L.; Angal, A.; Bhatt, R. Characterization of Terra and Aqua MODIS VIS, NIR, and SWIR spectral band calibration stability. *IEEE Trans. Geosci. Remote Sens.* **2012**, *51*, 4330–4338. [[CrossRef](#)]
6. Loeb, N.G.; Doelling, D.R.; Wang, H.; Su, W.; Nguyen, C.; Corbett, J.G.; Liang, L.; Mitrescu, C.; Rose, F.G.; Kato, S. Clouds and the Earth's Radiant Energy System (CERES) Energy Balanced and Filled (EBAF) Edition 4.0 Data Products. *J. Clim.* **2017**, under review.
7. Loeb, N.G.; Wielicki, B.A.; Su, W.; Loukachine, K.; Wong, T.; Priestley, K.J.; Matthews, G.; Miller, W.F.; Davies, R. Multi-Instrument Comparison of Top-of-Atmosphere Reflected Solar Radiation. *J. Clim.* **2007**, *20*, 575–591. [[CrossRef](#)]
8. Bhatt, R.; Doelling, D.R.; Wu, A.; Xiong, X.; Scarino, B.R.; Haney, C.O.; Gopalan, A. Initial Stability Assessment of S-NPP VIIRS Reflective Solar Band Calibration Using Invariant Desert and Deep Convective Cloud Targets. *Remote Sens.* **2014**, *6*, 2809–2826. [[CrossRef](#)]
9. Platnick, S.; Li, J.Y.; King, M.D.; Gerber, H.; Hobbs, P.V. A solar reflectance method for retrieving the optical thickness and droplet size of liquid water clouds over snow and ice surfaces. *J. Geophys. Res.* **2001**, *106*, 15185–15199. [[CrossRef](#)]
10. Meyer, K.; Platnick, S. Utilizing the MODIS 1.38 mm channel for cirrus cloud optical thickness retrievals: Algorithm and retrieval uncertainties. *J. Geophys. Res.* **2010**, *115*, D24209. [[CrossRef](#)]
11. Hu, Y.; Wielicki, B.; Yang, P.; Stackhouse, P.; Lin, B.; Young, D. Application of deep convective cloud albedo observations to satellite-based study of terrestrial atmosphere: Monitoring stability of space-borne measurements and assessing absorption anomaly. *IEEE Trans. Geosci. Remote Sens.* **2004**, *42*, 2594–2599.
12. Doelling, D.R.; Morstad, D.L.; Scarino, B.R.; Bhatt, R.; Gopalan, A. The characterization of deep convective clouds as an invariant calibration target and as a visible calibration technique. *IEEE Trans. Geosci. Remote Sens.* **2013**, *51*, 1245–1254. [[CrossRef](#)]
13. Wang, W.; Cao, C. DCC Radiometric Sensitivity to Spatial Resolution, Cluster Size, and LWIR Calibration Bias Based on VIIRS Observations. *J. Atmos. Ocean. Technol.* **2015**, *32*, 48–60. [[CrossRef](#)]
14. Mu, Q.; Wu, A.; Xiong, X.; Doelling, D.R.; Angal, A.; Chang, T.; Bhatt, R. Optimization of a Deep Convective Cloud Technique in Evaluating the Long-Term Radiometric Stability of MODIS Reflective Solar Bands. *Remote Sens.* **2017**, *9*, 535. [[CrossRef](#)]
15. Bhatt, R.; Doelling, D.R.; Angal, A.; Xiong, X.; Scarino, B.; Gopalan, A.; Haney, C.; Wu, A. Characterizing response versus scan-angle for MODIS reflective solar bands using deep convective clouds. *J. Appl. Remote Sens.* **2017**, *11*, 016014. [[CrossRef](#)]
16. Bhatt, R.; Doelling, D.R.; Scarino, B.R.; Gopalan, A.; Haney, C.O.; Minnis, P.; Bedka, K.M. A consistent AVHRR visible calibration record based on multiple methods applicable for the NOAA degrading orbits, Part I: Methodology. *J. Atmos. Ocean. Technol.* **2016**, *33*, 2499–2515. [[CrossRef](#)]

17. Doelling, D.R.; Bhatt, R.; Scarino, B.R.; Gopalan, A.; Haney, C.O.; Minnis, P.; Bedka, K.M. A consistent AVHRR visible calibration record based on multiple methods applicable for the NOAA degrading orbits, Part II: Validation. *J. Atmos. Ocean. Technol.* **2016**, *33*, 2517–2534. [[CrossRef](#)]
18. Doelling, D.R.; Wu, A.; Xiong, X.; Scarino, B.R.; Bhatt, R.; Haney, C.O.; Morstad, D.; Gopalan, A. The radiometric stability and scaling of collection 6 Terra- and Aqua-MODIS VIS, NIR, and SWIR spectral bands. *IEEE Trans. Geosci. Remote Sens.* **2015**, *53*, 4520–4535. [[CrossRef](#)]
19. Chang, T.; Xiong, X.; Angal, A.; Mu, Q. Assessment of MODIS RSB detector uniformity using deep convective clouds. *J. Geophys. Res. Atmos.* **2016**, *121*, 4783–4796. [[CrossRef](#)]
20. Doelling, D.R.; Haney, C.O.; Scarino, B.R.; Gopalan, A.; Bhatt, R. Improvements to the geostationary visible imager ray-matching calibration algorithm for CERES Edition 4. *J. Atmos. Ocean. Technol.* **2016**, *33*, 2679–2698. [[CrossRef](#)]
21. Morstad, D.L.; Doelling, D.R.; Bhatt, R.; Scarino, B. The CERES calibration strategy of the geostationary visible channels for CERES cloud and flux products. In Proceedings of the SPIE 8153, Earth Observing Aystem XVI, San Diego, CA, USA, 14 September 2011.
22. Wang, W.; Cao, C. Monitoring the NOAA Operational VIIRS RSB and DNB Calibration Stability Using Monthly and Semi-Monthly Deep Convective Clouds Time Series. *Remote Sens.* **2016**, *8*, 32. [[CrossRef](#)]
23. Doelling, D.R.; Morstad, D.L.; Bhatt, R.; Scarino, B. Algorithm Theoretical Basis Document (ATBD) for Deep Convective Cloud (DCC) Technique of Calibrating GEO Sensors with Aqua-MODIS for GSICS, GSICS. 2011. Available online: [http://gsics.atmos.umd.edu/pub/Development/AtbdCentral/GSICS\\_ATBD\\_DCC\\_NASA\\_2011\\_09.pdf](http://gsics.atmos.umd.edu/pub/Development/AtbdCentral/GSICS_ATBD_DCC_NASA_2011_09.pdf) (accessed on 24 August 2017).
24. Suttles, J.T.; Green, R.N.; Smith, G.L.; Staylor, W.F.; Wielicki, B.A.; Walker, I.J.; Young, D.F.; Taylor, V.R.; Stowe, L.L. Angular Radiation Models for Earth-Atmosphere System Volume I—Shortwave Radiation. Available online: <https://ntrs.nasa.gov/search.jsp?R=19880018293> (accessed on 13 October 2017).
25. Loeb, N.G.; Kato, S.; Loukachine, K.; Manalo-Smith, N. Angular Distribution Models for Top-of-Atmosphere Radiative Flux Estimation from the Clouds and the Earth’s Radiant Energy System Instrument on the Terra Satellite. Part I: Methodology. *J. Atmos. Ocean. Technol.* **2005**, *22*, 338–351. [[CrossRef](#)]
26. Tobin, D.C.; Revercomb, H.E.; Moeller, C.C.; Pagano, T.S. Use of Atmospheric Infrared Sounder high-spectral resolution spectra to assess the calibration of Moderate resolution Imaging Spectroradiometer on EOS Aqua. *J. Geophys. Res.* **2006**, *111*, D09S05. [[CrossRef](#)]
27. Moeller, C.; Tobin, D.; Quinn, G. S-NPP VIIRS thermal band spectral radiance performance through 18 months of operation on-orbit. *Proc. SPIE* **2013**, 8866. [[CrossRef](#)]
28. Hong, G.; Yang, P.; Heidinger, A.K.; Pavolonis, M.J.; Baum, B.A.; Platnick, S.E. Detecting opaque and nonopaque tropical upper tropospheric ice clouds: A trispectral technique based on the MODIS 8–12 mm window bands. *J. Geophys. Res.* **2010**, *115*, D20214. [[CrossRef](#)]



© 2017 by the authors. Licensee MDPI, Basel, Switzerland. This article is an open access article distributed under the terms and conditions of the Creative Commons Attribution (CC BY) license (<http://creativecommons.org/licenses/by/4.0/>).